Galaxy Survey Cosmology, additional material for part 2

Hannu Kurki-Suonio

16.4.2021

Contents

Preface

The lecture notes for the second part of Galaxy Survey Cosmology are still mostly hand written; here is some additional material mainly related to recent observations.

– Hannu Kurki-Suonio, April 2019/2021

1   Black holes

Motivated by the recently published image of the supermassive black hole in the center of the M87 galaxy in the Virgo cluster, obtained with the Event Horizon Telescope [1], we discuss gravitational lensing by a black hole.

1.1   Schwarzschild black holes surrounded by empty space

Let us first review some basic features of Schwarzschild, i.e., non-rotating, black holes. This simplest kind of black hole is spherically symmetric and static. In terms of the Schwarzschild coordinates, the spacetime metric is

$$ds^2 \; = \; -\left(1 - \frac{2GM}{r}\right) dt^2 + \left(1 - \frac{2GM}{r}\right)^{-1} dr^2 + r^2 d\theta^2 + r^2 \sin^2\theta d\phi^2 \,, \tag{1}$$

where M is the black hole mass. At $r = R_S \equiv 2GM$, the *Schwarzschild radius*, there is an *event horizon*, from inside which there are no paths out. Circular orbits around the black hole have coordinate velocity $v_{\mathrm{coord}} \equiv r d\phi/dt = \sqrt{GM/r}$. The coordinate time t corresponds to the time of an observer at rest (infinitely) far from the black hole. An observer located at the orbit, at fixed r, θ, ϕ measures time $d\tau = \sqrt{1 - 2GM/r}\,dt$, so that she observers the orbital speed to be

$$v = r\frac{d\phi}{d\tau} = \sqrt{\frac{GM}{r}}\frac{dt}{d\tau} = \sqrt{\frac{GM}{r - 2GM}} \,. \tag{2}$$

This physical speed increases as the orbital radius is decreased, and reaches the speed of light, $v = c = 1$, at $r = 3GM$. This means that photons can orbit the black hole at $r = 3GM$, and that orbits of massive particles must have $r > 3GM$. Smallest such orbits, and the circular photon orbit, turn out to be unstable. The innermost stable circular orbit (ISCO) is at $r = 6GM = 3R_S$, with orbital speed $v = c/2$.

Consider now light rays approaching the black hole with different impact parameters b. The light rays are bent by the black hole (well, they travel as straight as possible in the curved spacetime, along lightlike geodesics, but drawn in the r, θ, ϕ coordinate system they appear bent), and it turns out that for $b < R_c \equiv \sqrt{27GM} \approx 5.196GM = 2.598R_S$, the *photon capture radius*, the photons will hit the event horizon and disappear in the black hole (see Fig. 1). For b close enough to R_c the photon will make several orbits around the black hole before either escaping, if $b > R_c$, or falling into the hole, if $b < R_c$. The case $b = R_c$ gives a photon path that asymptotically approaches the (unstable) photon orbit at $r = 3GM$.

For a slightly larger impact parameter, $b = R_r \approx 5.34GM$, we have the case where the photon goes exactly half way around the black hole and comes out from the other side of the black hole heading back to the direction it came from. This means that you can see the black hole by shining a powerful light at it: some of the light will return to you, and you will see it as a circle around the black hole [2]. There will actually be an infinite sequence of concentric, fainter, circles corresponding to rays that went $\frac{1}{2}$, $\frac{3}{2}$, $\frac{5}{2}$ etc. times around the black hole; the outermost with radius $b = R_r$, and the sequence approaching radius $b = R_c$. In practice, we might not resolve the circles separately, so that they would rather appear as a single *photon ring* with inner radius R_c and outer radius R_r.

In [2], Holz&Wheeler proposed that we could this way detect a nearby stellar-mass black hole as it returned the light of the Sun. This requires an alignment with the Sun, the observer, and the black hole, to accuracy given by the size of the Sun in the sky, $0.5°$ if the observer is on the Earth or near Earth's orbit. They calculate that the returning light from the black hole at distance d would appear with magnitude

$$m \; = \; 30 + 2.5\lg\left[\left(\frac{d}{0.02\mathrm{pc}}\right)^3 \left(\frac{M}{10M_\odot}\right)^{-2}\right] \,. \tag{3}$$
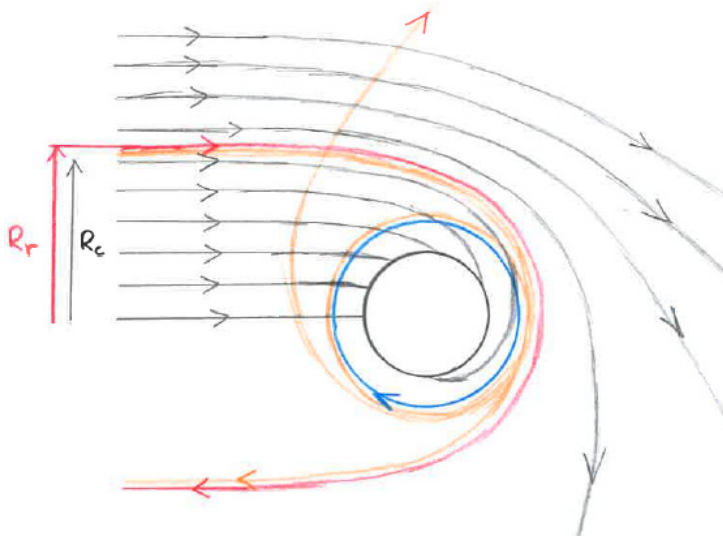
Figure 1: Parallel light rays approaching the black hole from the left, with different impact parameters. For an impact parameter b less than the photon capture radius R_c, the photons are swallowed by the black hole. If $b = R_c$, the photons end up orbiting the black hole, asymptotically approaching the black hole photon orbit (blue). For a slightly larger impact parameter, $b = R_r$, the photon ring radius, the photons go half way around the black hole and are returned to the direction they came from (red). For $R_c < b < R_r$, the photons go around the black hole by more than half a circle before leaving it (the two orange rays).

Thus a typical stellar-mass black hole with $M = 10M_\odot$ at $d = 0.02\,\text{pc}$ would have magnitude $m = 30$, and would be observable with the Hubble Space Telescope (HST)[1]. Such objects could be searched in the same way as the microlensing searches for MACHOs, since the returned light from the black hole would have a characteristic light curve, as it and the observer move in and out of alignment with the Sun. It is very unlikely that there would be such a black hole so near to the Solar System. It is more probable that the closest black hole is more than 10 pc away. The diameter of the photon ring of a $M = 10M_\odot$ black hole is about 160 km. Even if it were 100 times closer, at $d = 0.0002\,\text{pc} = 41\,\text{AU}$, near the orbit of Pluto, where it would completely disrupt the planetary orbits, the apparent diameter of the photon ring would be just 5 mas, so we couldn't resolve the ring, and it would appear as a point source.[2]

Forget now about shining a light at the black hole, assume that there are no light sources near the black hole, or between the black hole and the observer, and consider how the black hole would appear to an observer as light from many distant sources (stars, galaxies) is bent near the black hole. From our earlier discussion of gravitational lensing around point masses, we have that sources directly behind them appear as an Einstein ring with angular radius

$$\theta_E = \sqrt{4GM\frac{D_{ds}}{D_dD_s}} \, . \tag{4}$$

In the limit, where the sources are infinitely far away, this becomes

$$\theta_E = \sqrt{\frac{4GM}{D_d}} \, . \tag{5}$$

Gravitational lensing thus opens an Einstein ring into the observer's view of the sky, so that the entire sky can be seen outside this ring. According to our earlier discussion there will be a

---

[1]The largest ground-based telescopes have limiting magnitude $m \approx 25$, limited by the atmosphere. HST has limiting magnitude $m \approx 31$

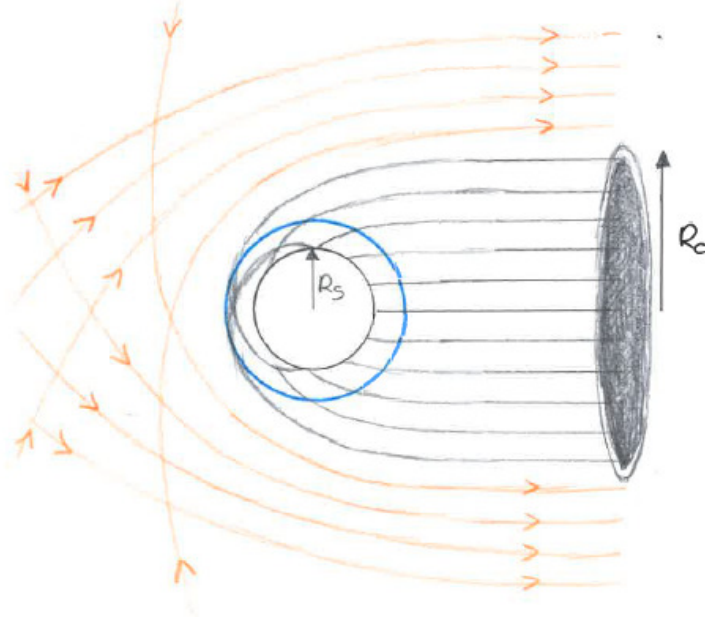[2]The resolution of HST is about 50 mas.

Figure 2: Observer lines of sight towards the black hole. The observer is far to the right. Lines of sight that end at the event horizon correspond to the black hole shadow, with radius R_c. Wrapped around this shadow (within the narrow ring drawn around the shadow) there are multiple images of the entire sky as seen from the vicinity of the black hole distorted into thin concentric rings, corresponding to light rays that have gone around the black hole half or more times.

second, inverted, image of the sky inside the Einstein ring. However, the earlier discussion was in the approximation of small bending angles, and when the light rays get close enough to the black hole the situation is modified. The Einstein ring radius around the black hole is

$$R_E = \theta_E D_d = \sqrt{4GM\frac{D_{ds}D_d}{D_s}} = \sqrt{\frac{2D_{ds}D_d}{D_s R_S}}R_S \tag{6}$$

(valid when D_d, D_s and D_{ds} are all $\gg R_s$). Let us work in the limit $D_s \gg D_d \gg R_S$. Then

$$R_E \approx \sqrt{\frac{2D_d}{R_S}}R_S \gg R_S\,. \tag{7}$$

Inside the Einstein ring the observer sees an inverted image of the sky, objects behind the black hole are seen close to the ring and objects further aside are seen further in. When we look closer to the black hole the bending angles get larger. As the observer is relatively distant from the black hole, we can consider all light rays that she will see as parallel, after they have left the vicinity of the black hole. Since the Schwarzschild metric is time-reversal symmetric, we can reuse the rays in Fig. 1 but reverse the direction the light is moving, see Fig. 2. The rays in the figure do not necessarily correspond to actual light rays: they are lines of sight corresponding to different pixels of the image the observer is seeing.

The rays that appear to come from closer than R_c from the black hole originate from the event horizon. What does this mean? Since no light is coming from inside the event horizon, these pixels will be completely black.[3] This is called the *black hole shadow*. Its radius is the photon capture radius $R_c \equiv \sqrt{27GM} \approx 5.196GM = 2.598R_S$.

---

[3]Suppose there are some light sources very close to the event horizon. The observer could then see them in the black hole shadow, but the closer to the event horizon they are, the longer it would take them, in observer time, to climb out of the gravitational well, and the more redshifted they would be. An astrophysical black hole would have formed at some time in the past, so technically the black hole shadow contains light rays coming from
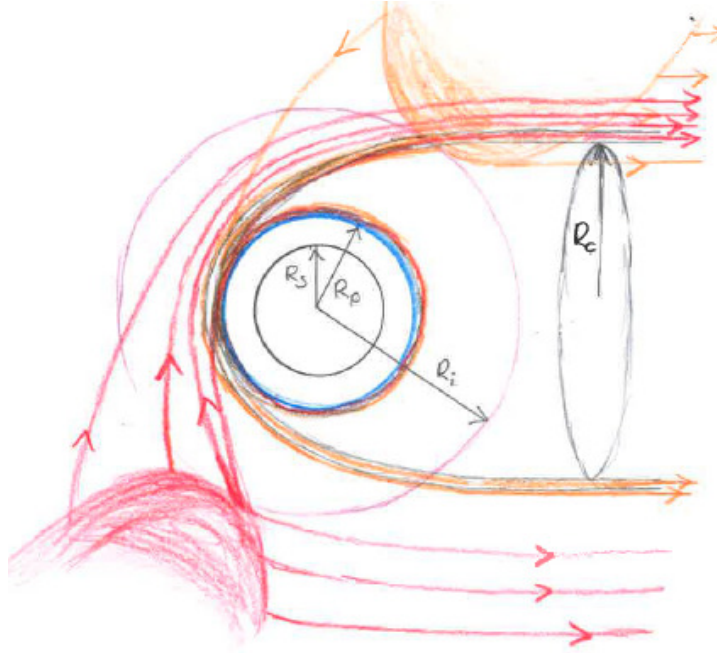
Figure 3: Cross section of a black hole system with a geometrically thick but optically thin disk. The upper (lower) part of the disk and some light rays from it that will reach the observer are colored orange (red). The observer is far to the right. With the rays that the disk sends towards the observer, the observer sees the disk almost as it is, the innermost parts appear just slightly shifted away from the hole by gravitational lensing. But also some of the rays sent away from the observer are bent towards her. Thus the observer will see the backside of the disk in or near the photon ring. Since we defined the photon ring radius R_r to correspond to photons that are turned 180° by the black hole, the rays from the backside of the lower part of the disk appear outside R_r, unless they make more than a full circle around the hole first, in which case they appear at $R_c < r < R_r$. A comparable amount (I don't know enough to be quantitative here) of light reaches the observer from the backside as from the front side of the disk, but the former is concentrated into a narrow ring in the image and would be conspicuous if we could resolve it. R_S is the Schwarzschild radius, R_p the photon orbit radius, R_c the photon capture (and black hole shadow) radius, R_r (not drawn) is the photon ring radius, and R_i is the radius of the innermost stable circular orbit, with $R_S < R_p < R_c < R_r < R_i$.

The entire sky around the black hole is mapped into the part of the image at $R_E > r > R_r$, inverted so that each part of the sky appears on the opposite side of the black hole[4]; and between this radius and R_c there is an infinite sequence of narrow rings, each an image of the full sky.

1.2   Schwarzschild black holes surrounded by accreting matter

Black holes are often surrounded by accretion disks of matter. This is made of matter that has fallen towards the black hole and has ended orbiting it. Particles acquire kinetic energy falling towards the black hole and reach relativistic speeds close to it. Particles orbiting the black hole collide with each other losing angular momentum and falling to lower orbits. These collisions also tend to align the orbital planes resulting in a disk orbiting the black hole. The

---

the progenitor star just before it was swallowed by the event horizon, but in practice these are so enormously redshifted that they are not visible. The purely mathematical Schwarzschild solution, where there is no such past history, can be extended to contain a *white hole* in the past, and the black hole shadow corresponds to the rays coming from this white hole; but this has nothing to do with astrophysical black holes.

[4]This image of the full sky has an outer boundary corresponding the radius at which parallel rays coming from behind the black hole are bent enough so that they converge to reach the observer. Outside it we see the "normal sky".
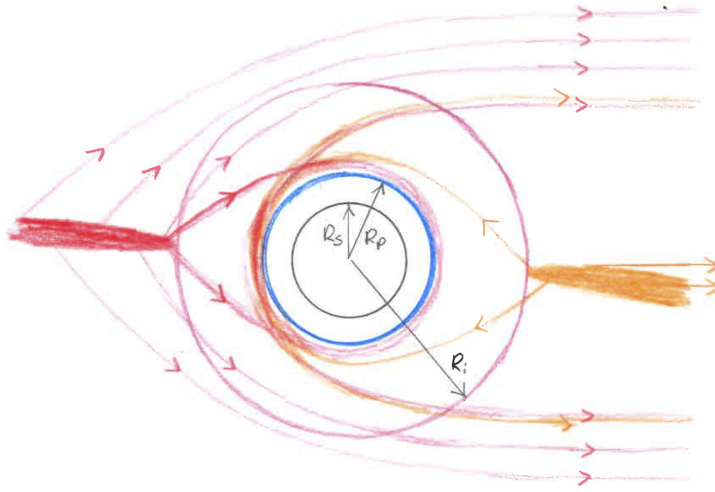
Figure 4: Cross section of a black hole system with a geometrically thin disk. The near (far) part of the disk and some light rays from it that will reach the observer are colored orange (red). The observer is far to the right. See Fig. 5 for how this looks to the observer.

inner boundary of the disk is the innermost stable orbit at $r = 6GM = 3R_S$. Particles falling inside it are rapidly swallowed by the black hole. Depending on the environment there may be more or less matter accumulated in the accretion disk. The higher the density of the disk, the more the particles collide with each other, and the flatter the disk becomes. The disk is a hot plasma of ions and electrons. Photons passing through the disk may be scattered especially by the electrons. The higher the density of the disk, the less transparent it will be to photons. We say the disk is optically thin (transparent), if most photons go through the disk without scattering, and optically thick (opaque) if most photons scatter (often many times) when going through the disk. Thus optical thickness is a completely different concept than geometrical thickness (shape) of the disk. In fact, geometrically thin disks tend to be optically thick, since they are related to higher density, and vice versa. Optical thickness is wavelength dependent.

Consider now a geometrically thick, optically thin, disk of hot matter around the black hole, tilted with respect to the line of sight so that it is closer to being transverse than parallel to it. See Fig. 3. The disk has a hole with radius $r = 3R_S$ (the innermost stable orbit), although there is some matter also further in that is falling into the black hole. We have drawn some light rays originating from the disk that will reach the observer. For the orientation drawn in Fig. 3, some light rays from the near side of the disk will cover a small piece of the black hole shadow. Also some of the radiation from matter (not drawn) falling into the black hole will appear within the shadow. Some light rays that the disk sends away from the observer go around the black hole and the observer sees them as a ring of light near the photon ring radius. Some of them go through the other side of the disk, so we need to assume the disk is optically thin for the observer to see them. There are also light rays that go several times around the black hole that the observer will see in the photon ring. This photon ring is characteristic of a black hole. It is not strictly necessary to have a black hole to produce a photon ring, but since these light rays pass very close to the photon orbit, the object must not be much larger than its photon orbit.

Consider then a geometrically thin, optically thick disk, close to parallel with the line of sight. See Fig. 4. The observer sees the near part of the disk almost as it is. Light from the part of the disk behind the event horizon is bent around the black hole so that the observer sees the top side of this part of the disk above the black hole and the bottom side below the black hole. In addition there are rays that are sent from both the near and far parts of the disk around the black hole that the observer sees as the photon ring. See Fig. 5 for how the black hole will
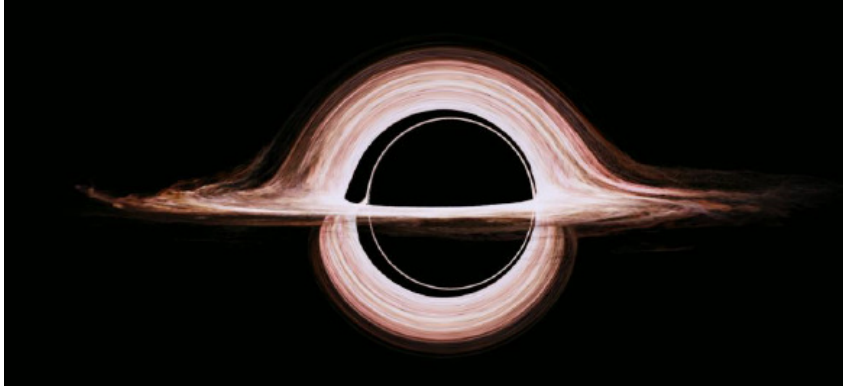
Figure 5: Image of a black hole with a thin accretion disk, as seen by an observer near the plane of the disk. From [3]. Note the thin photon ring inside the more direct image of the accretion disk. This image is left-right asymmetric, since it is actually for a rotating black hole – however, the brightening of the side that is moving towards the observer is ignored here; see Fig. 6 for how a rotating black hole would really look like.
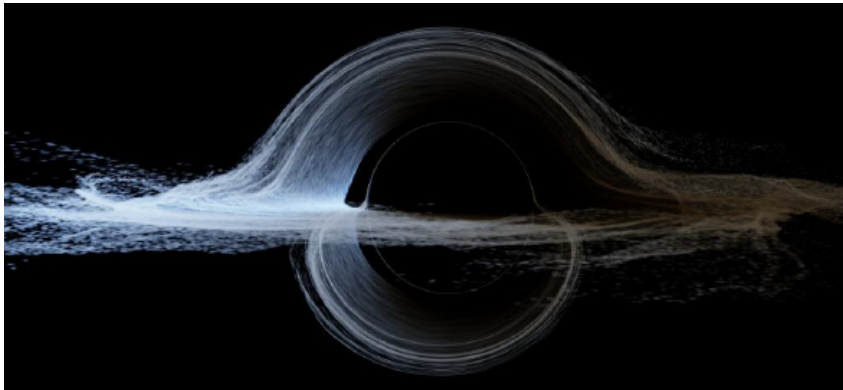

Figure 6: Image of a rotating black hole with a thin accretion disk, as seen by an observer near the plane of the disk. From [3]. The side that is moving towards the observer appears brighter than the side that is moving away.

appear.

1.3   Kerr black holes

In reality, all black holes rotate: they are Kerr black holes, not Schwarzschild black holes. Exact calculations are much more complicated for Kerr black holes, so we give just some qualitative results. The spacetime geometry is no longer spherically symmetric, so we have to distinguish between the equatorial plane, axis, and other directions. The rotation "drags" the spacetime in the direction of rotation, pulling particles and photons in this direction.

In the equatorial plane there are now two (unstable) circular photon orbits, an inner one orbiting in the black hole rotation direction (prograde) and an outer one in the opposite direction (retrograde). There are also photon orbits off the equatorial plane, but they have more complicated shapes. The rotation makes the black hole shadow slightly smaller (diameter 4.5–$5.2R_S$) and noncircular and it is not centered around the black hole but somewhat shifted.

The accretion disk around the Kerr black hole may rotate either in the same direction as the black hole or in the opposite direction. A prograde disk is more likely, since the black hole pulls infalling matter in this direction, but a retrograde disk is also possible if the environment has a suitably oriented flow of matter towards the black hole. These systems have also *jets*, matter

being ejected from the system in the direction of the rotation axis, powered by the magnetic field caused by the moving charges in the accretion disk.

See Fig. 6 for how a rotating black hole with a thin accretion disk would appear to an observer near the plane of the disk.

1.4 The EHT image of the supermassive black hole in M87

True images of black holes are difficult to obtain, since black holes are small compared to their distance from us. The two known black holes with the largest angular sizes as seen from the Solar System are Sagittarius A* (Sgr A*) and M87*.

Sgr A* is the black hole at the center of Milky Way, 8 kpc from here. Its mass is about 4 million solar masses, corresponding to a Schwarzschild radius of 12 million km. The diameter of the black hole shadow is thus 60 million km or 0.4 AU, which seem from 8 kpc corresponds to an angle of 50 μas (microarcsecond).

M87* is much farther away, at the center of the massive elliptical galaxy M87 in Virgo cluster. The distance to M87* is 16.8 ± 0.8 Mpc and its mass is $(6.5 \pm 0.7) \times 10^9 \, M_\odot$ [1], so that its 2100 times farther away, but also 1600 times larger than Sgr A*; leading to a black hole shadow of 40 μas in diameter.

The angular resolution of a telescope is λ/L, where L is the diameter of the telescope and λ is the wavelength of radiation observed. With radio interferometry observations from different radio telescopes can be combined to achieve an effective diameter given by the distance (baseline) between the telescopes. With ground-based telescopes the maximum effective diameter is thus the diameter of the Earth; in practice somewhat less, since the telescopes must observe the object simultaneously and the object must be above the horizon for all of them. Resolution is higher for shorter wavelengths, and the shortest wavelengths than can currently be used for long-baseline radio interferometry are of the order of a millimeter. Long-baseline interferometry is based on recording the observations of the different telescopes and combining them computationally afterwards. This requires very precise matching of the timing of the observations, achieved with atomic clocks at each telescope, and the positions of the telescopes need to be known with an accuracy better than the wavelength used. This is not feasible for optical wavelengths, for which also the computational task would be enormous. Instead, optical interferometry can be done by physically combining light coming from different nearby telescopes, and the longest baselines achieved this way are a few hundred meters. Thus, in practice, radio interferometry can currently achieve better resolution.

The Event Horizon Telescope is an array of about a dozen radio telescope stations (some with multiple telescopes) around the world. In their 2017 campaign eight[5] stations at six different geographic locations participated in simultaneous observations of M87* at 1.3 mm wavelength during four different April nights. See Fig. 7. Each pair formed a baseline; the longest baseline was 10 700 km and the shortest 160 m. Thus the resolution achieved was 1.3 mm / 10 700 km = 25 μas. Interferometry does not produce a direct image; instead, comparing the data from a pair of telescopes measures a single Fourier component of the image, determined by the orientation and length of the baseline (as the Earth rotates, the orientation changes, and thus a sequence of nearby Fourier components is obtained).

The more telescopes at different locations participate, the more Fourier components can be solved, but they will anyway form an incomplete set for uniquely determining the image. See Fig. 7. Thus image reconstruction requires some assumptions about the image. Fig. 8 show preliminary images of M87* obtained by four independent teams making different assumptions. Although there are differences between these images, they all show a ring with the same size,

---

[5]Two older EHT stations had been decommissioned prior to 2017, and three newer ones had not yet joined.
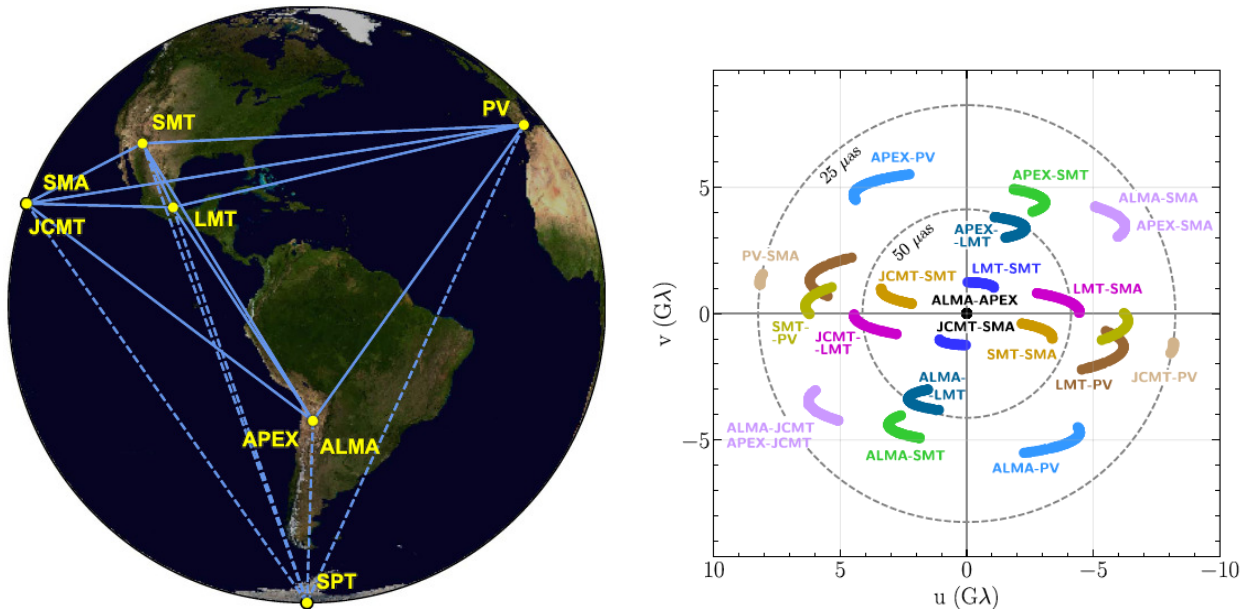
Figure 7: Left: The EHT stations that participated in the 2017 campaign. The solid baselines were used for the observation of M87*. It is not visible from the South Pole, so SPT was used only for calibration. Right: The different Fourier components of the image towards M87* obtained by EHT. From [1].
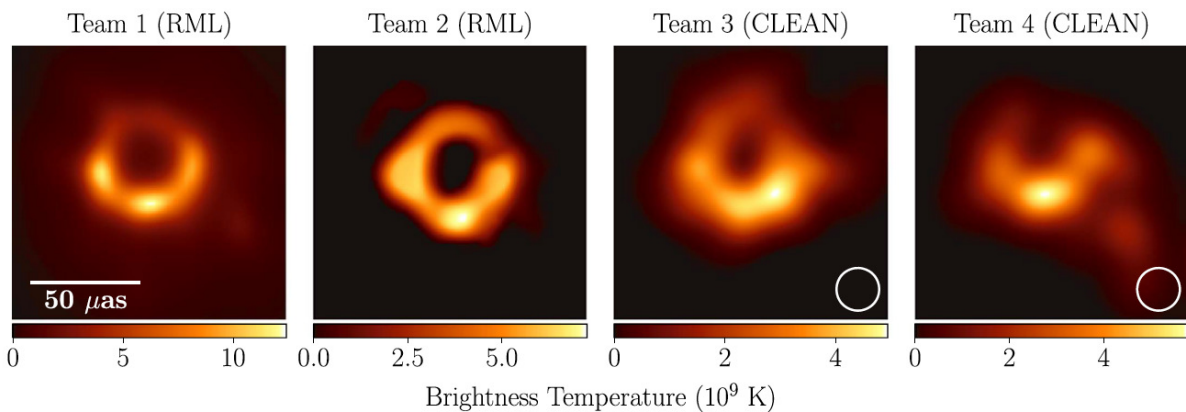

Figure 8: Preliminary images of M87* obtained by four independent teams within the EHT Collaboration, making different assumptions, from an early release of the April 11 observation data. The two images on the right have been smoothed with a 20 μas beam (the white circle gives its size). Only one polarization component of the data was used for these preliminary images, whereas the final image (Fig. 10) used total intensity. From [4].
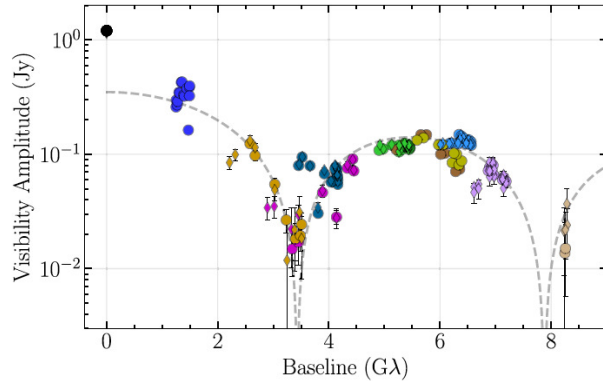
Figure 9: The amplitude of the different measured Fourier components compared to those of a symmetric thin ring with diameter $46\,\mu$as (dashed line). From [1].

brighter in the south, and dark in the center. The ring size is thus a clean measurement of EHT, see Fig. 9.

The final published image of M87* from the four different observing nights is shown in Fig. 10. It is smoothed with a $20\,\mu$as beam to remove sub-resolution artifacts of the image reconstruction. The image corresponds to what we would expect for a black hole whose accretion disk is not far from perpendicular to the line of sight, so that its near side does not get in front of the black hole shadow. This is like the system in Fig. 3. The disk is geometrically thick and optically thin, and it is made of hot plasma (ions and electrons). The radiation at $1.3\,$mm wavelength is synchrotron radiation from the electrons in the plasma. The rotation axis must be tilted somewhat away from the line of sight, since the south (north) side of the ring is brighter (fainter), indicating motion towards (away from) us. The direction of the rotation axis of the black hole is known from the orientation of the jet ejected from the system (observed already a long time ago at much larger scales)[6], which is to the west of being towards us. Combined with this information the image indicates that the black hole is rotating clockwise. With this resolution we cannot distinguish the narrow photon ring from the more direct wider image of the accretion disk. The size of M87* corresponds to a dynamical time scale of a day, so there could be changes in the disk between the observing nights, but since the image is largely determined by the spacetime geometry around the black hole, which is unchanging, it is not surprising that the four images look very similar.

Because the resolution is not much better than the size of the image, not much more information beyond the size and orientation of the system can be obtained from it. At this resolution simulations of quite different physical models lead to similar images (Fig. 11). Some possibilities can be excluded, however: Black holes with $|a_*| > 1$ do not have an event horizon and are called *naked singularities*.[7] These would have smaller shadows and more asymmetric images, so we can rule this case out for M87*. While the simulation with $a_* = 0$, i.e., a non-rotating black hole, with just the accretion disk rotating around it (middle column in Fig. 11), produces an acceptable fit to the obtained image, rotation of the black hole is required to power the jet from M87*. In the case of retrograde rotation of the accretion disk, the EHT team concludes from the simulations that the asymmetry of the image is determined by the black hole spin (i.e., the black hole must spin clockwise), which forces also part of the plasma to rotate prograde.[8]

---

[6]There is a YouTube video https://youtu.be/C628xyDN40o showing a sequence of observations of M87* at different resolutions zooming in to this new image; the older, lower resolution, images show mainly the jet.

[7]It is usually assumed that these would be so difficult to form that they do not exist.

[8]This is my interpretation of what the papers [1, 4, 5, 6] say about the black hole spin and disk rotation, but they are not very clear in this; the statement that the image asymmetry is determined by the orientation of the black hole spin seems contradictory to the statement that we would get a similar image from a non-spinning black
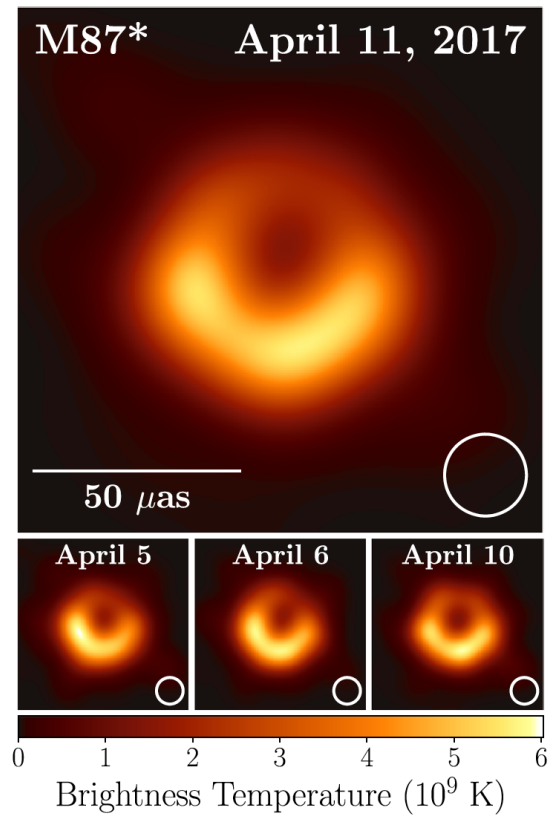
Figure 10: The final published images of M87*, smoothed with a 20 μas beam. North is up and east is to the left. From [1].
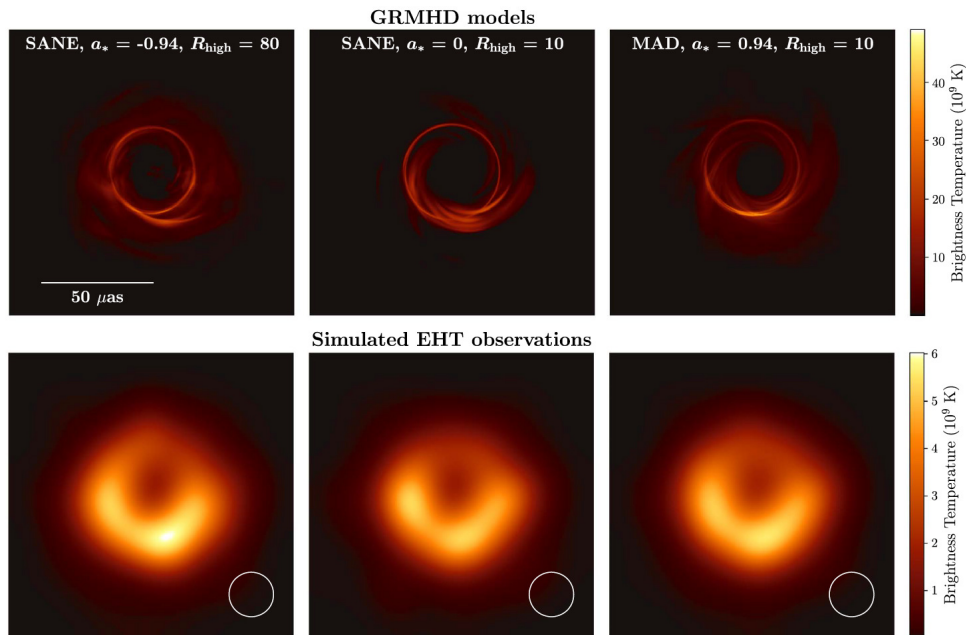

Figure 11: Images produced from simulations of three different physical models of the M87* system. SANE and MAD are different models for the accretion disk, with different magnetization, and different relative strength of emission from the disk vs from the jet; R_{high} is related to the electron and ion temperatures in the plasma; and a_* is the black hole spin in units of GM^2, negative value indicating that the accretion disk rotates in the opposite direction. Top: high-resolution images. Bottom: smoothed with a 20 μas beam. From [1].

Earlier estimates of the mass of the M87* object were $6.2^{+1.1}_{-0.6} \times 10^9 M_\odot$ from the motion of stars around it and $3.5^{+0.9}_{-0.3} \times 10^9 M_\odot$ from motion of gas. The size of the image obtained with EHT tells that this mass is concentrated in a region comparable in size to its Schwarzschild radius and is dark in the center, as for a black hole. Thus it is strong evidence in favor of the system indeed being a black hole with surrounding plasma. In principle, we could imagine modifications to GR that could make this object somewhat different from a GR black hole, or modifications to other physics allowing the existence of dark objects slightly larger than their event horizon. Assuming the object is a GR black hole, we get from the size of the image a more precise and reliable mass estimate, $(6.5 \pm 0.7) \times 10^9 \, M_\odot$, for it.
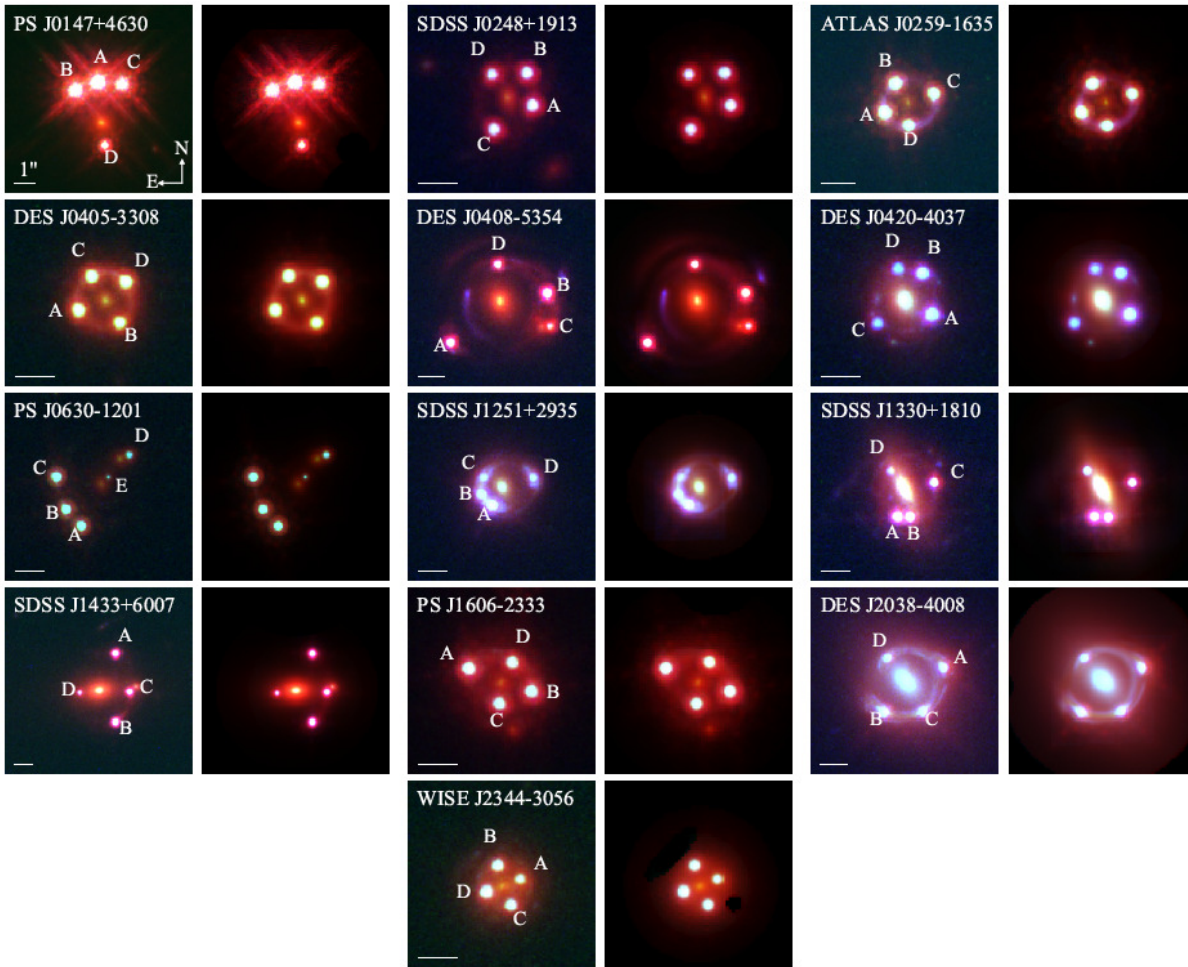
---

hole.

Figure 12: Strong gravitational lens systems with quadruply (A, B, C, and D) imaged quasars. Because of the odd-number theorem, there should actually be 5 images, but only for the PS J0630-1201 system the fifth image (E) is large enough to be seen. The 1st, 3rd, and 5th column are Hubble Space Telescope images; the 2nd, 4th, and 6th columns are reconstructions based on modeling the lens and the source. From [7].

2   Strong lensing

In Fig. 12 we show Hubble Space Telescope images of strong gravitational lens systems with quadruply imaged quasars (quads), together with reconstructed images based on modeling the lens and the source.
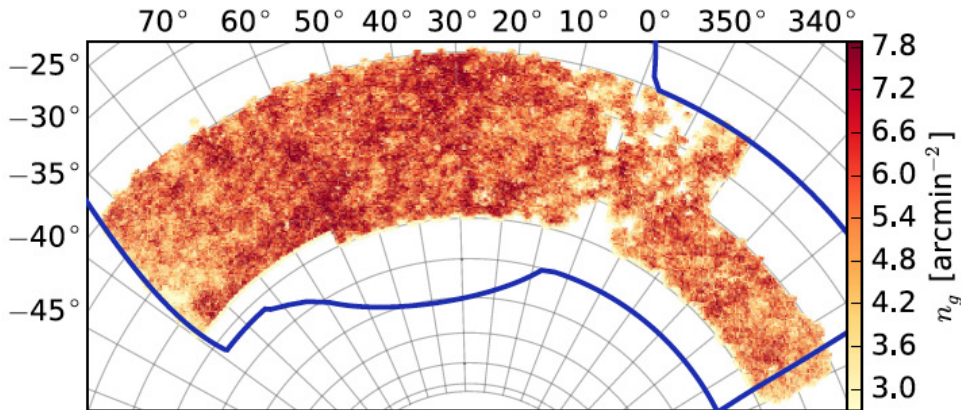
Figure 13: The 1321 deg^2 region of sky used for the DES first-year cosmic shear correlation measurement. The color gives the number of used galaxy images per square arcmin of sky. The dark blue thick line indicates the nominal DES survey region for the full 6-year project. From [10].

3 Results from cosmological weak lensing surveys

(For now, we present just DES results, since they are currently (2019) the best. KiDS (Kilo-Degree Survey) released their "KiDS-1000" (1000 square degrees; actually 1006 square degrees of data; after masking 777 square degrees used for cosmology) results in 2020 [8]; they are of comparable quality to the DES 1-year results. We are now (April 2021) waiting for the release of DES 3-year results.)

Observational cosmology with weak lensing is still (in 2021) in its infancy and much more impressive results are expected during the next decade. The most important weak lensing survey that has already published results is the Dark Energy Survey (DES). It was a six-year survey that began on August 31, 2013 and ended taking data on January 9, 2019, having surveyed 5000 deg^2 of sky and observed over 300 million galaxies. It used a 570-megapixel digital camera on a 4-meter telescope in Chile. In 2017, they released their first-year results covering 1786 deg^2 [9].

3.1 Shear correlation function and cosmological parameters

DES divided the observed galaxies into 4 redshift bins,

$$z = [(0.2 - 0.43), (0.43 - 0.63), (0.63 - 0.9), (0.9 - 1.3)] , \tag{8}$$

and used 26 million good-quality galaxy images, within a 1321 deg^2 region (see Fig. 13), to estimate the shear correlation functions in each bin, and also cross-correlations between bins, see Fig. 14.

If one assumes a ΛCDM model, the cosmological parameters the cosmological shear is most sensitive to, are the amplitude A_s of the primordial power spectrum and Ω_m, which affects the growth of structure. For galaxy surveys it is customary to use σ_8, the rms mass fluctuation in linear theory at $8\,h^{-1}$Mpc scale, instead of A_s. The constraints on Ω_m and σ_8 turn out to be correlated; this correlation can be broken if instead of σ_8 one uses the parameter

$$S_8 \equiv \sigma_8 \left(\frac{\Omega_m}{0.3} \right)^{0.5} \tag{9}$$

(the reference value 0.3 is just to make S_8 to have a value close to σ_8, as Ω_m is known to be close to 0.3), which can be determined more accurately than σ_8 itself. Fig. 15 shows the DES constraints on these parameters.
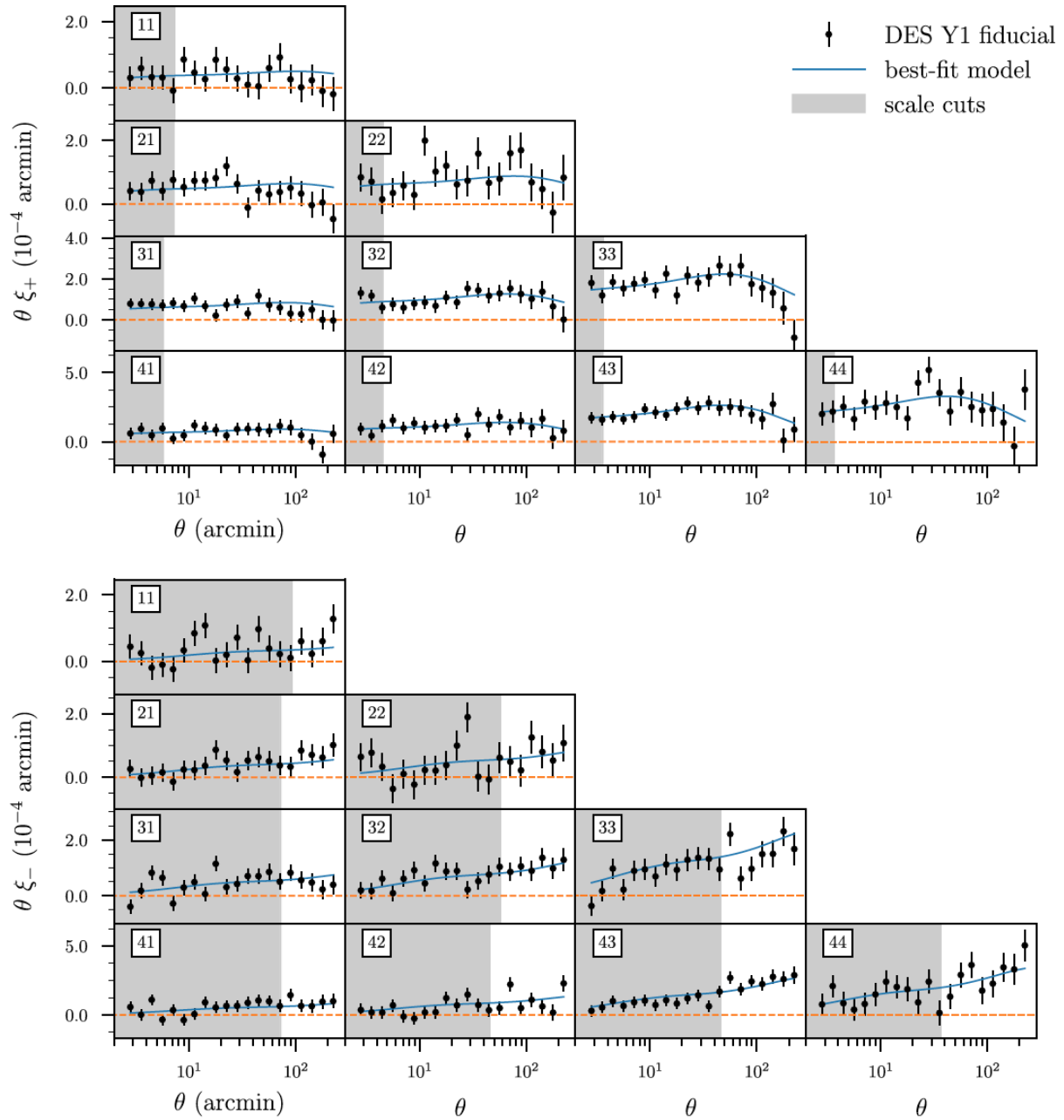
Figure 14: The shear correlation functions $\xi_+(\theta)$ and $\xi_-(\theta)$ in 4 redshift bins, and also shear cross-correlations between bins, from DES 1st year results. The blue solid lines are predictions from their best-fit ΛCDM model. The shaded regions were not used for determining cosmological parameters. From [9].
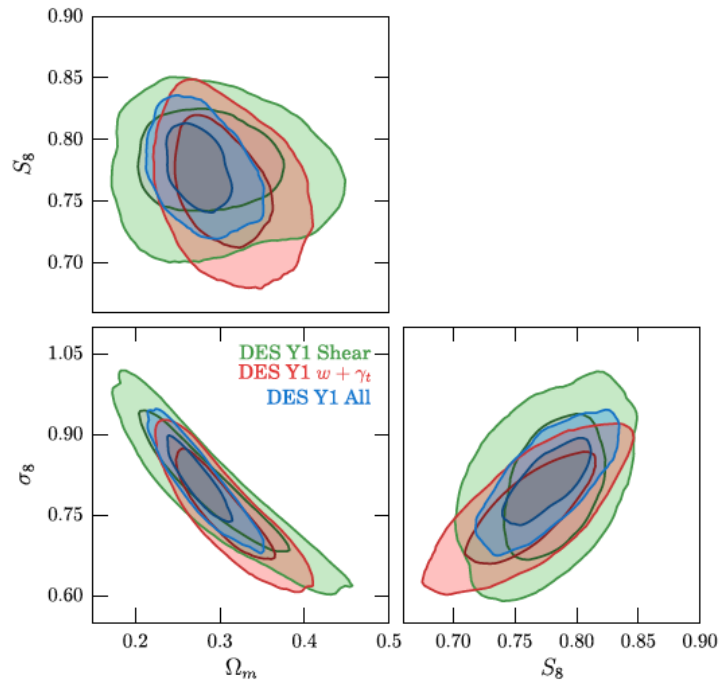
Figure 15: The constraints on the ΛCDM parameters Ω_m, σ_8, and S_8 from DES 1st year results. The green areas are constraints from cosmic shear, the red areas are from galaxy clustering, and the blue areas combine both cosmological probes. The inner contours are 68% confidence levels and the outer contours 95%. From [9].
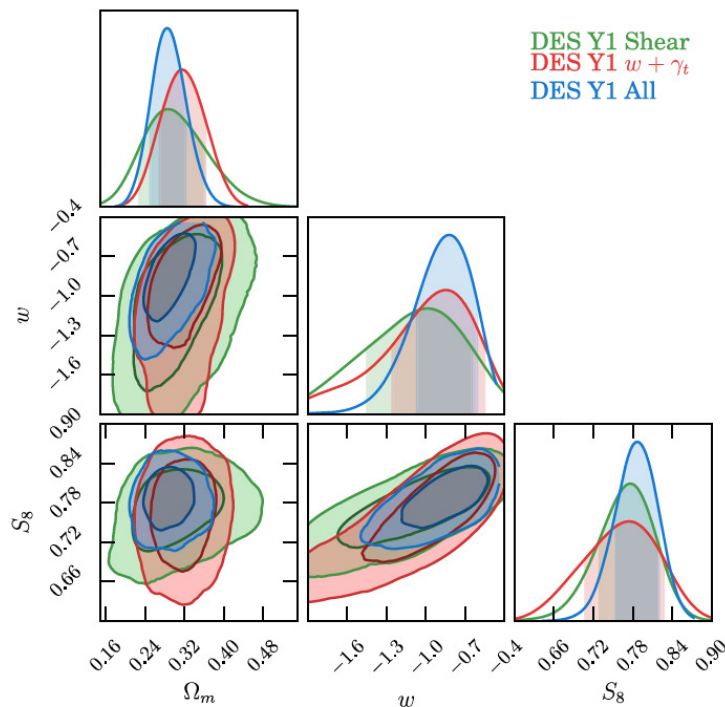

Figure 16: Constraints on the wCDM parameters Ω_m, w, and S_8 from DES 1st year results. From [9].
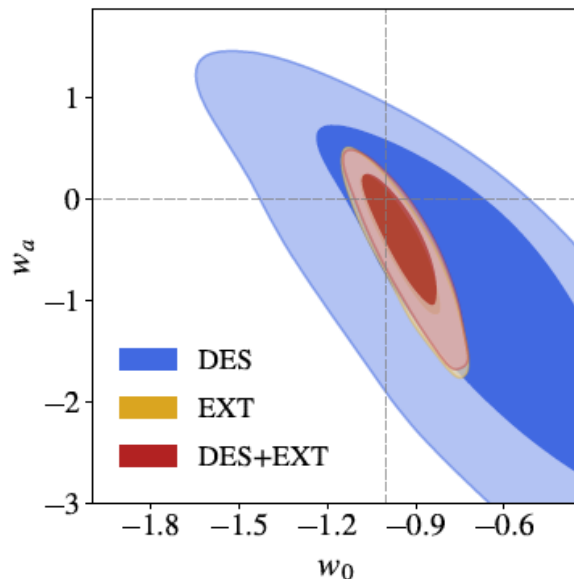
Figure 17: Constraints on the dark energy parameters w_0 and w_a from DES 1st year results and other (EXT) cosmological data. From [11].

The future goal of cosmic shear surveys is to constrain dark energy, so as a first step, DES considered the wCDM model, where the cosmological constant Λ of ΛCDM is replaced with the very simple dark energy model of a constant equation-of-state parameter $w \equiv p/\rho$. The (not yet very impressive) DES 1st year constraints on the wCDM model are shown in Fig. 16.

The next step is to constrain a two-parameter model for the dark energy equation of state,

$$w(a) \;=\; w_0 + (1-a)w_a \,, \tag{10}$$

where w_0 is the present ratio of dark energy pressure to dark energy density, and w_a is its derivative with respect to the scale factor a. The even less impressive DES constraints on them are shown in Fig. 17, together with constraints from other existing cosmological data (Planck data on the cosmic microwave background; baryon acoustic oscillation measurements from SDSS, 6dF, and BOSS galaxy surveys; redshift-space distortion from BOSS; and type Ia supernova data). For now, this other kind of data does a much better job on constraining dark energy; but the situation should change with the "Stage IV" weak lensing surveys of the 2020s: Euclid, the Legacy Survey of Space and Time (LSST) of the Vera Rubin Observatory (formerly called the Large Synoptic Survey Telescope), the Square Kilometer Array (SKA), and the NASA Roman Space Telescope (formerly called the Wide Field Infrared Survey Telescope (WFIRST)).

3.2 Mass maps

Using the Fourier space relation

$$\kappa(\mathbf{l}) \;=\; \frac{D^*(\mathbf{l})\gamma(\mathbf{l})}{\pi}\,, \qquad \text{where} \quad D(\mathbf{l}) \;=\; \pi\,\frac{l_1^2 - l_2^2 + 2il_1l_2}{l^2} \tag{11}$$

one can obtain the convergence κ in Fourier space from shear measurements. With inverse Fourier transform one then obtains a sky map of the convergence, i.e., of the weighted mass density along the line of sight projected on the sky. DES published earlier such a "mass" map of $139\,\mathrm{deg}^2$ of sky, see Fig. 18. Such mass maps have limited resolution, since a large number of galaxies is needed to obtain sufficient statistics for a shear measurement. Fig. 19 shows how the method works for simulated data.
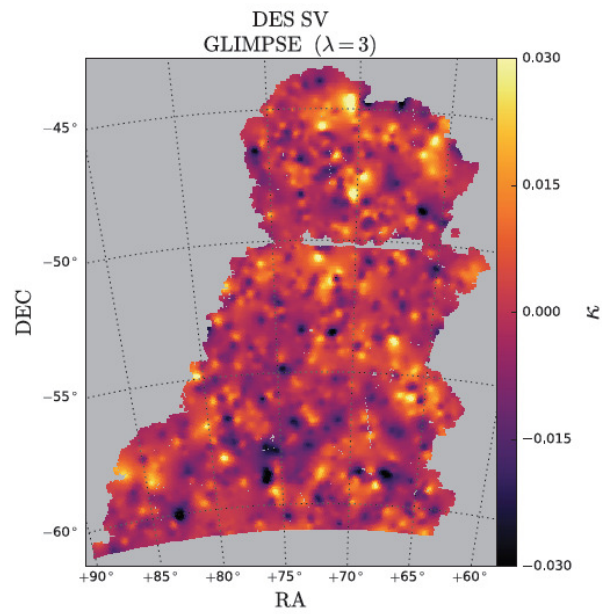
Figure 18: Convergence map from DES Science Verification data. Orange and yellow are overdensities, purple and black underdensities. A smoothing scale of 10 arcmin was used. From [12].
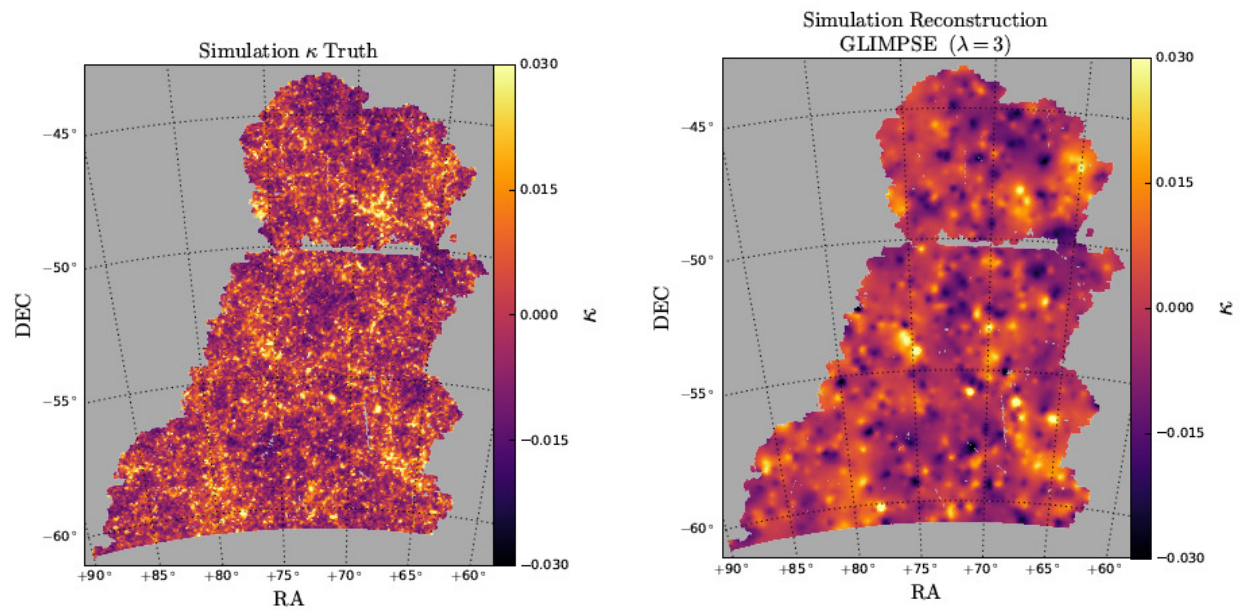

Figure 19: Left: True convergence map of simulated data. Right: Reconstructed convergence map from simulated shear observations of this simulated data. From [12].
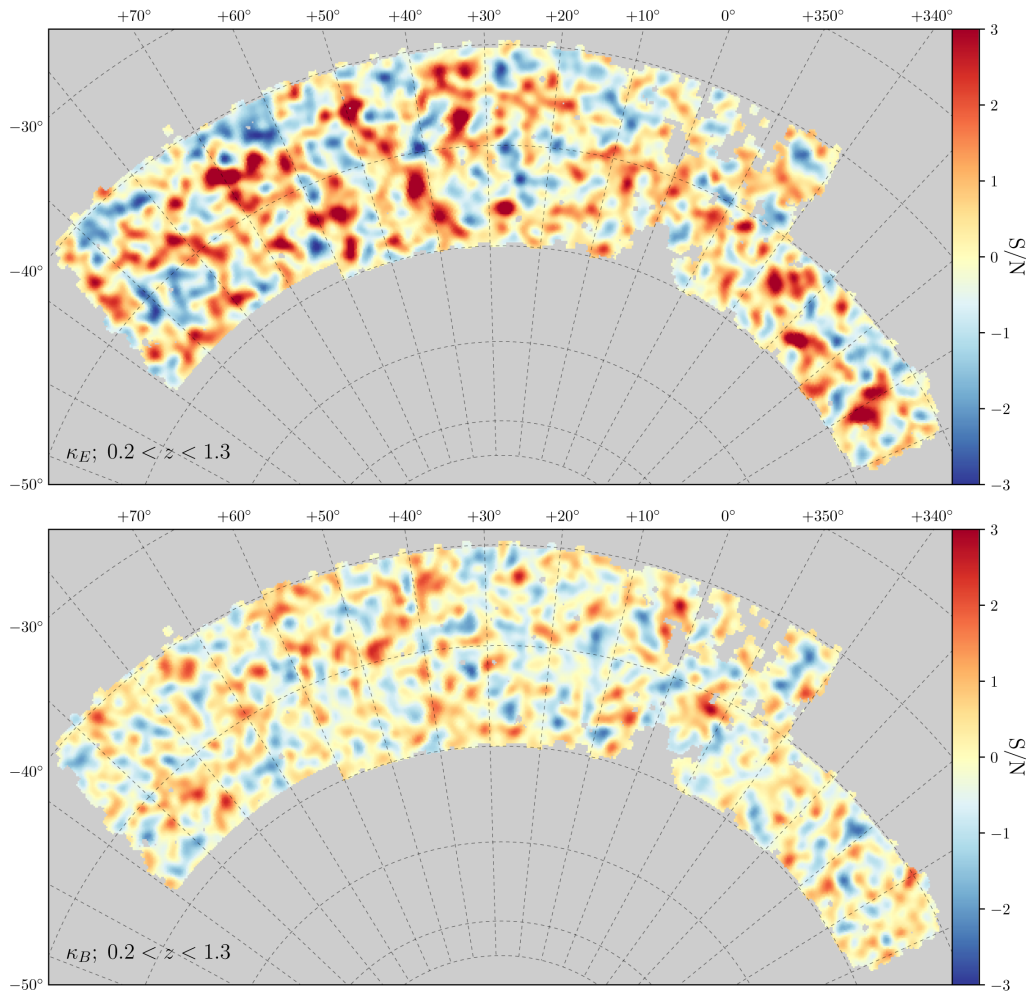
Figure 20: The DES 1-year mass map. The top panel shows the κ_E convergence map, which is an estimate of the projected mass along the line of sight (weighted so that mass halfway between us and the observed galaxies (which have redshifts in the range $0.2 < z < 1.3$) has the most weight). The bottom panel shows the κ_B convergence map, which is mostly estimation noise. Both images are smoothed with a 30 arcmin Gaussian filter. From [13].

The DES 1-year mass map is shown in Fig. 20. It shows the estimated integrated mass density between us and the DES galaxies weighted by the $D_d^A D_{ds}^A / D_s^A$ distance factor. To get information about the distribution of mass along the line-of-sight direction ("tomography"), the same is done separately for the four redshift bins of DES galaxies in Fig. 21
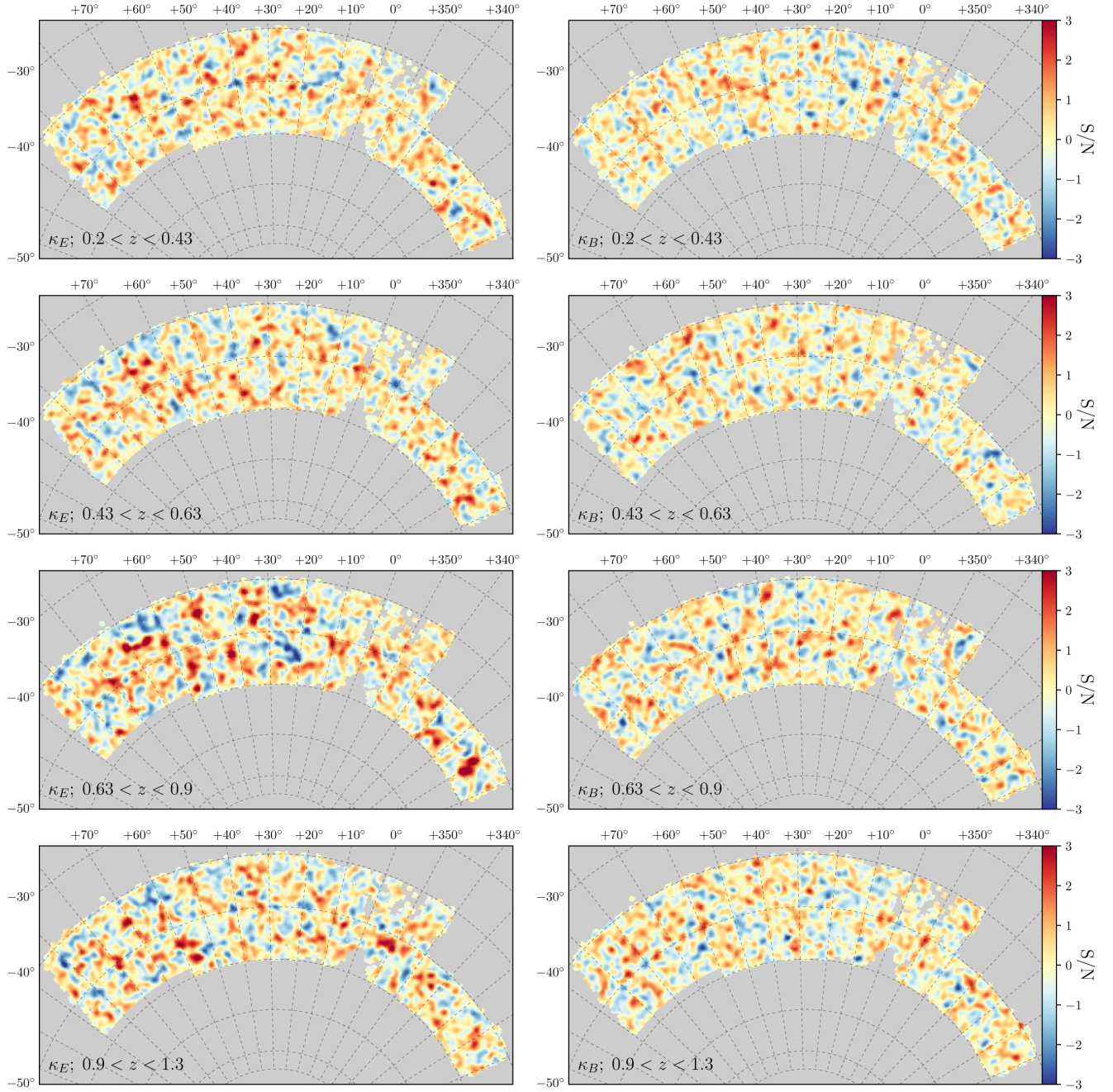
Figure 21: The DES 1-year tomographic mass maps for the four redshift bins. The κ_E convergence maps (mass estimate) are on the left and the κ_B convergence maps (mainly noise) on the right. Note that the redshifts are for the galaxy images, and the mass is between us and these galaxies. Because there are now fewer galaxies per map the estimation noise is higher than in Fig. 20. From [13].

4   CMB lensing

We have not discussed gravitational lensing of the cosmic microwave background (CMB), but the principle is the same. CMB is expected to be statistically isotropic, so if we see the patterns in it elongated in a particular direction in some region of the sky, this indicates that the CMB photons have been gravitationally lensed by the intervening mass distribution. Thus we can this way obtain an estimate of the projected mass between us and the CMB (weighted by the $D_d^A D_{ds}^A / D_s^A$ distance factor). The redshift of the CMB, $z = 1090$, is much higher than that of galaxies and corresponds to the edge of the observable universe. Thus CMB lensing gives us an account of all mass in the whole observable universe. The patterns in the CMB are much larger, several arcmin across, than galaxy images or separations between nearby galaxy images, so the mass map obtained from CMB lensing has a much poorer angular resolution. See Figs. 22 and 23.
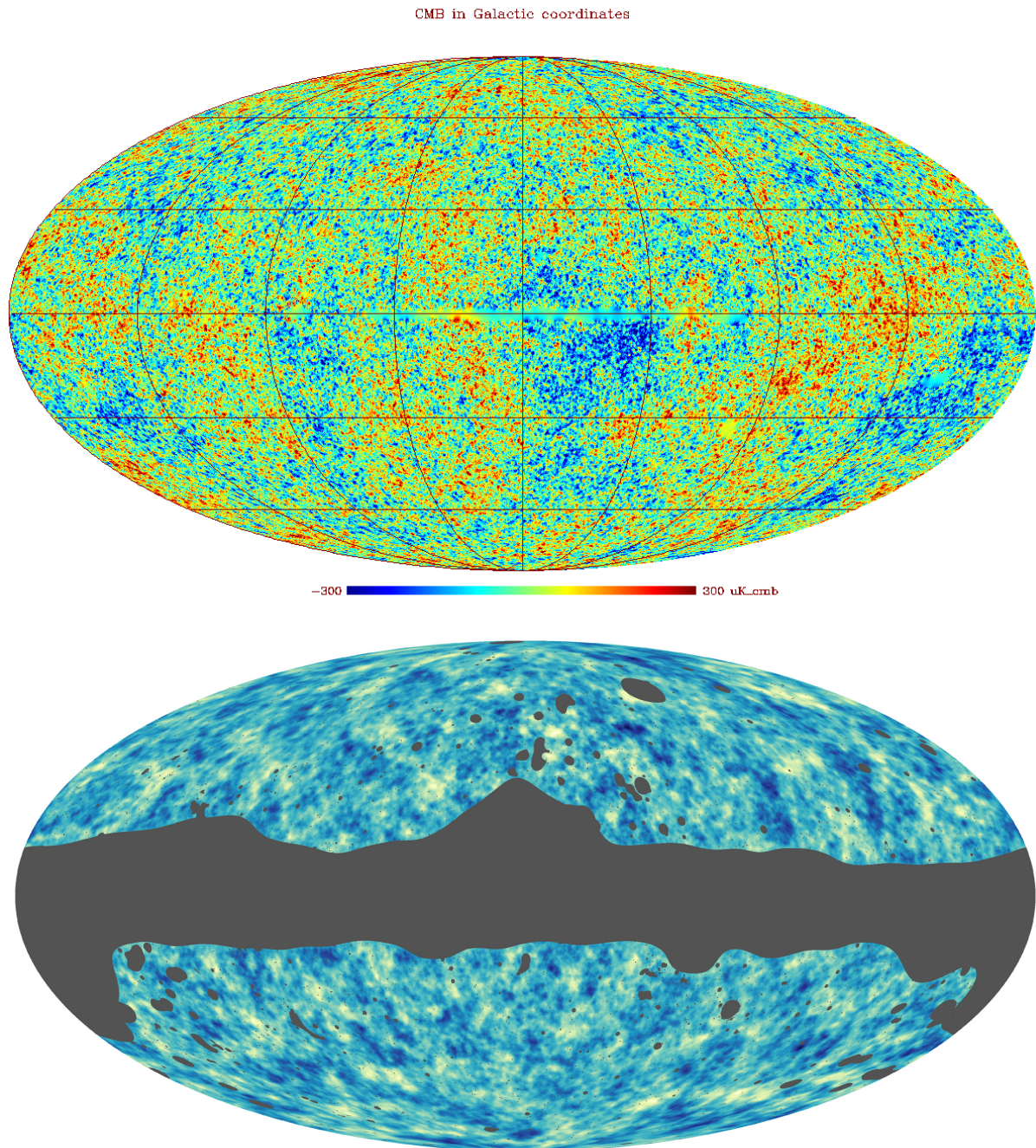
CMB in Galactic coordinates

Figure 22: Top panel: Cosmic microwave background as observed by Planck. The color range corresponds to CMB temperature variations from $-300\,\mu\text{K}$ (blue) to $+300\,\mu\text{K}$ (red) around the mean temperature. (ESA/Planck data). Bottom panel: The mass map obtained from lensing of the CMB. Darker color corresponds to overdensity and lighter color to underdensity. The dark gray areas have been excluded from the analysis due to foreground contamination of the CMB. From [14].
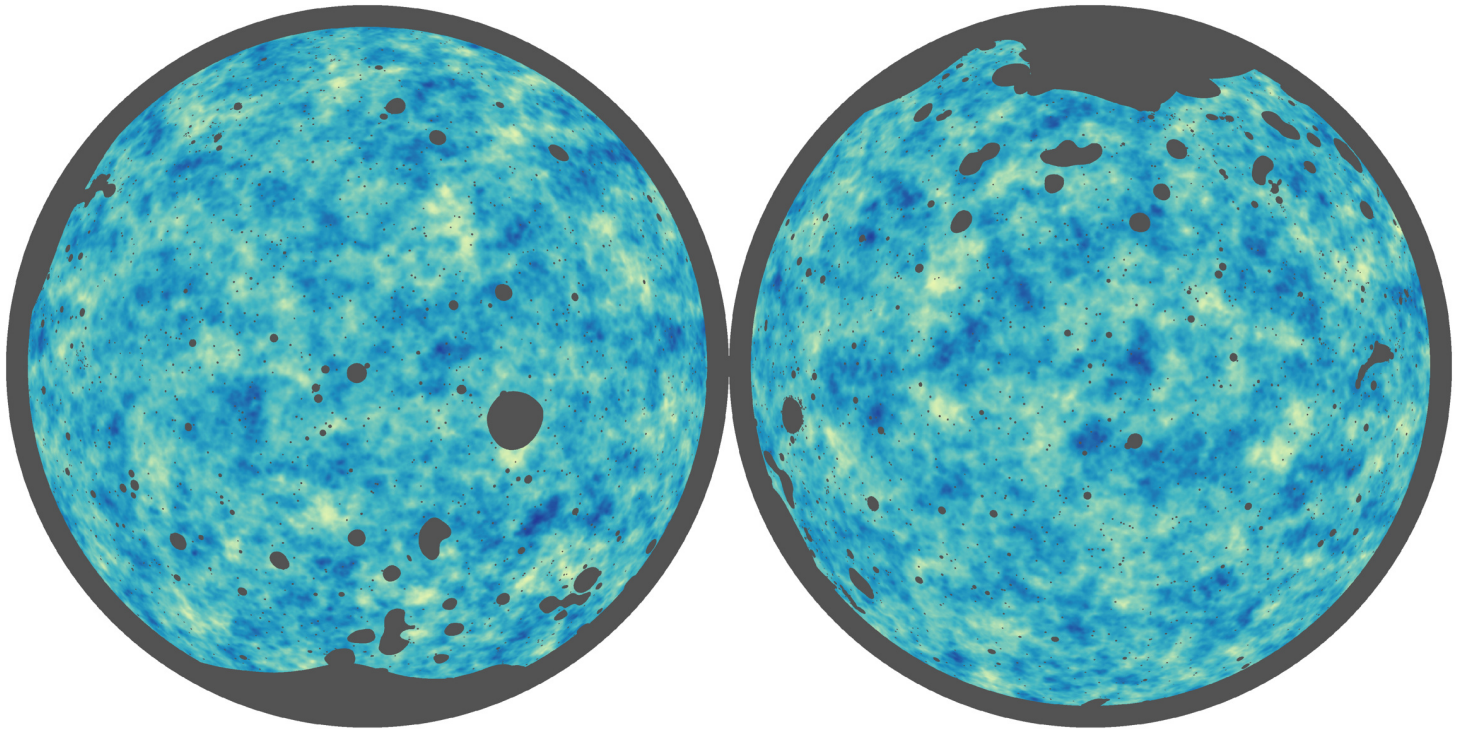
Figure 23: Total mass distribution in the observed universe. This figure is the same as bottom panel of Fig. 22, but in a different projection showing the northern galactic hemisphere on the left and the southern on the right. From [14].

References

[1] The Event Horizon Telescope Collaboration, *First M87 Event Horizon Telescope Results. I. The Shadow of the Supermassive Black Hole*, ApJL **875**, L1 (2019)

[2] D.E. Holz, J.A. Wheeler, *Retro-MACHOs: π in the Sky?*, ApJ **578**, 330 (2002)

[3] O. James, E. von Tunzelmann, P. Franklin, and K.S. Thorne, *Gravitational Lensing by Spinning Black Holes in Astrophysics, and in the Movie Interstellar*, arXiv:1502.03808, Classical and Quantum Gravity **32**, 065001 (2015)

[4] The Event Horizon Telescope Collaboration, *First M87 Event Horizon Telescope Results. IV. Imaging the Central Supermassive Black Hole*, ApJL **875**, L4 (2019)

[5] The Event Horizon Telescope Collaboration, *First M87 Event Horizon Telescope Results. V. Physical Origin of the Asymmetric Ring*, ApJL **875**, L5 (2019)

[6] The Event Horizon Telescope Collaboration, *First M87 Event Horizon Telescope Results. VI. The Shadow and Mass of the Central Black Hole*, ApJL **875**, L6 (2019)

[7] A.J. Shajib et al., *Is every strong lens model unhappy in its own way? Uniform modelling of a sample of 13 quadruply+ imaged quasars*, arXiv:1807.09278

[8] C. Heymans et al., *KiDS-1000 Cosmology: Multi-probe weak gravitational lensing and spectroscopic galaxy clustering constraints*, arXiv:2007.15632v2

[9] Dark Energy Survey Collaboration, *Dark Energy Survey year 1 results: Cosmological constraints from galaxy clustering and weak lensing*, PRD **98**, 043526 (2018), arXiv:1708.01530

[10] Dark Energy Survey Collaboration, M.A. Troxel et al., *Dark Energy Survey year 1 results: Cosmological constraints from cosmic shear*, PRD **98**, 043528 (2018), arXiv:1708.01538

[11] Dark Energy Survey Collaboration, *Dark Energy Survey year 1 results: Constraints on extended cosmological models from galaxy clustering and weak lensing*, arXiv:1810.02499

[12] Dark Energy Survey Collaboration, N. Jeffrey et al., *Improving weak lensing mass map reconstructions using Gaussian and sparsity priors: Application to DES SV*, arXiv:1801.08945

[13] DES Collaboration, C. Chang et al., *Dark Energy Survey Year 1 results: curved-sky weak lensing mass map*, MNRAS **475**, 3165 (2018)

[14] Planck Collaboration, *Planck 2018 results VIII. Gravitational lensing*, A&A **641**, A8 (2020)